中国激光

基于纳米颗粒热效应的飞秒激光高效直写金属铜微结构

崔梦雅，黄婷*，肖荣诗

北京工业大学材料与制造学部，北京 100124

摘要 在 $Cu(NO_3)_2$ 前驱体溶液中添加硅纳米颗粒，采用飞秒激光在透明基底表面成功直写了导电金属铜微结构。前驱体溶液中的硅颗粒作为吸光粒子吸收激光能量后对溶液进行加热，使 Cu^{2+} 还原为金属铜并沉积在基底表面。结果表明：当激光光强为 5.32×10^9～8.51×10^9 $W\cdot cm^{-2}$、扫描速度为 100～500 $mm\cdot s^{-1}$ 时，微结构主要由铜、Cu_2O 及微量硅组成，铜含量及微结构的导电性随着光强的增加或扫描速度的降低而逐渐增加；在光强为 5.32×10^9 $W\cdot cm^{-2}$、扫描速度为 100 $mm\cdot s^{-1}$ 的条件下，铜微结构的方阻为 0.28 $\Omega\cdot sq^{-1}$，电阻率为 4.67×10^{-6} $\Omega\cdot m$。与已有的飞秒激光直写铜微结构的技术相比，这种方法使激光光强降低了 2 个数量级，直写效率提高了 1～3 个数量级。

关键词 激光技术；飞秒激光；激光直写技术；吸光粒子；铜微结构；导电性

中图分类号 TN249 **文献标志码** A **doi**：10.3788/CJL202249.0802015

1 引 言

在透明基底表面制造的薄膜形式的导电图案在信息电子、物质检测、能源存储等领域具有广阔的应用前景[1-3]。目前，制备导电图案的最常见方法包括光刻法、印刷电路法、喷墨打印等[4-6]，这些方法通常包含多个加工步骤，不仅增加了制备时间，还降低了成品率。因此，如何在透明基底表面高效、可靠地制备金属图案成为人们关注的焦点[7-8]。

目前，基于光热效应或光化学效应的激光直写技术已成为一种无需掩模、加工精度高、可简单快速地在基底表面制造金属微结构的先进技术[9-10]。其中：基于光热效应的金属微结构激光直写技术利用激光束辐照材料时产生的热量使材料发生烧结或诱导材料发生物理、化学变化，从而实现金属结构的制造[11-14]；而基于光化学效应的金属结构激光直写技术利用前驱体材料中因吸收光子而跃迁到激发态的电子在返回基态过程中产生的键断裂与键生成，在化学反应过程中实现金属离子的还原。目前，基于光化学效应的金属结构激光直写技术主要是利用飞秒激光的双光子吸收效应实现金属离子的还原，即有机光敏分子在光斑焦点处发生非线性吸收，金属离子被受激的电子还原为金属单质并沉积在基底表面[15-17]。

与其他金属材料相比，铜具有良好的导电和导热性能，同时其自然界储量丰富、成本低，已成为广泛应用的金属材料之一。已有研究表明，激光直写过程中反应区域的温度决定了金属铜的含量，而且直写结构的导电性与铜含量呈正相关[18]。玻璃、聚酰亚胺(PI)等材料的透明基底对反应区域的温度比较敏感，过高的温度会损伤基底表面[19-21]。因此，精确控制反应区域的温度对控制金属铜含量以及避免破坏基底具有重要意义。与连续、普通脉冲或短脉冲激光相比，超快激光的脉宽极短（10^{-13}～10^{-15} s），可以精确控制热输入，从而可以实现直写过程中反应区域温度的精确控制[22-24]。Mizoshiri 等[25]和廖

收稿日期：2021-08-27；**修回日期**：2021-09-28；**录用日期**：2021-10-21

基金项目：国家自然科学基金(51975018)

通信作者：*huangting@bjut.edu.cn

嘉宁等[26]分别利用飞秒激光诱导还原不同成分的Cu^{2+}/聚乙烯吡咯烷酮(PVP)薄膜制造出了导电的铜微结构。尽管飞秒激光可以精确控制激光的热输入量,但为了满足Cu^{2+}还原所需的温度,要求飞秒激光的光强极高,至少需要达到10^{11} W·cm^{-2}量级;飞秒激光的加工速度慢,直写速度一般小于10 mm·s^{-1}。因此,在透明基底表面低成本、高效率地制造导电性良好的金属微结构仍然是一项极具挑战性的工作。

本课题组提出了一种基于纳米颗粒热效应的飞秒激光直写金属铜微结构的方法,即在$Cu(NO_3)_2$前驱体溶液中添加硅纳米颗粒(Si NPs),硅纳米颗粒以线性方式吸收激光能量并加热其周围溶液,将Cu^{2+}还原为金属铜。该方法可使直写光强降低至10^9 W·cm^{-2}量级。本文研究了激光光强和扫描速度对激光直写铜微结构形貌和物相的影响,并对金属微结构的导电性进行了分析。

2 试验条件与方法

2.1 试验材料

前驱体溶液由 6 mL 乙二醇、3 mL 去离子水、4 g $Cu(NO_3)_2\cdot 3H_2O$ 混合配制而成。首先将溶液搅拌 30 min 以上使$Cu(NO_3)_2$充分溶解,然后将液体加热至 170 ℃,保温 2 min,待溶液静置至室温后,向溶液中添加 100 mg 纳米硅颗粒(直径约为100 nm),并在水浴中持续超声 1 h,以获得均匀性良好的悬浮液。将玻璃基底置于配制好的悬浮液的上表面,使悬浮液与基底背部完全接触。

2.2 飞秒激光直写系统

采用 TruMicro 5280 Femto Edition 飞秒激光器(TRUMPF)和 hurrySCAN Ⅱ 14 振镜系统(Scanlab)进行直写。激光波长为 515 nm,脉宽为800 fs,频率为 600 kHz,最高激光功率为 75 W,最小激光功率为 1.5 W。场镜焦距为 f=255 mm,焦点直径为 50 μm。飞秒激光直写过程示意图如图 1 所示,激光经过振镜系统后聚焦在加工平台上,通过计算机程序对激光器和振镜系统进行控制,激光穿过玻璃基底后在基底和悬浮液界面处扫描,得到设定图案的金属结构。

2.3 表征与测试

分别采用 Olympus GX51 光学显微镜(OM)和GeminiSEM 300 场发射扫描电子显微镜(SEM)观察样品表面的微结构及形貌。控制激光的扫描路径,扫描区域的填充间距等于光斑直径,激光直写后

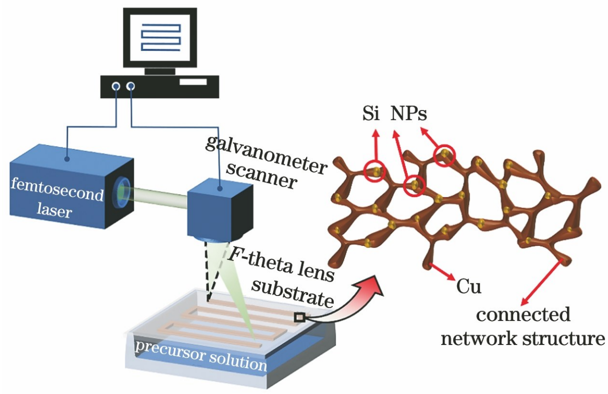

图 1 飞秒激光直写铜微结构系统示意图

Fig. 1 Schematic of femtosecond laser direct writing of Cu microstructures system

形成 10 mm×10 mm 的二维微结构区域。利用LabX XRD-6100 型 X 射线衍射仪(XRD)表征微结构的成分,XRD 的测试条件为:铜靶,扫描速度2 (°)·min^{-1},扫描范围 20°~80°。利用 WykoNt1100表面轮廓仪测量微结构的厚度,并绘制三维形貌。采用 BEST-300C 四探针测试仪测量所得结构的电学性能。

3 结果与讨论

3.1 光强对铜微结构形貌及物相的影响

为了验证本文所提方法,即采用飞秒激光在低光强下直写金属微结构的方法,需要降低光强。由于本文采用的飞秒激光器的最小输出功率为1.5 W,焦点直径为 50 μm,焦点处的光强过高,因此采用正离焦的方式,通过增大光斑来降低光强,即:离焦量为 15 mm,光斑直径为 306 μm。当以500 mm·s^{-1}的扫描速度重复扫描 50 次时,不同光强下铜微结构的 OM 照片及 SEM 照片如图 2 所示。当光强为 5.32×10^9 W·cm^{-2} 时,仅能从前驱体溶液中还原出分散的铜纳米颗粒,在基底表面沉积了少量材料。当激光光强增大至 7.45×10^9 W·cm^{-2} 时,溶液中还原出的铜含量增加,基底表面形成了连续的微结构。直写微结构的线宽随着激光光强的增加而逐渐增大,当光强为 8.51×10^9 W·cm^{-2} 时,微结构的线宽为 213 μm,小于光斑直径(306 μm)。进一步利用 SEM 观察微结构的表面形貌,结果发现激光在不同光强下直写的微结构整体上比较相似,均呈三维网络状。

图 3 所示为激光直写微结构的 XRD 图谱。微结构主要由不同比例的金属铜及Cu_2O组成。其中43.3°、50.4°和74.1°处的三个衍射峰分别与铜的

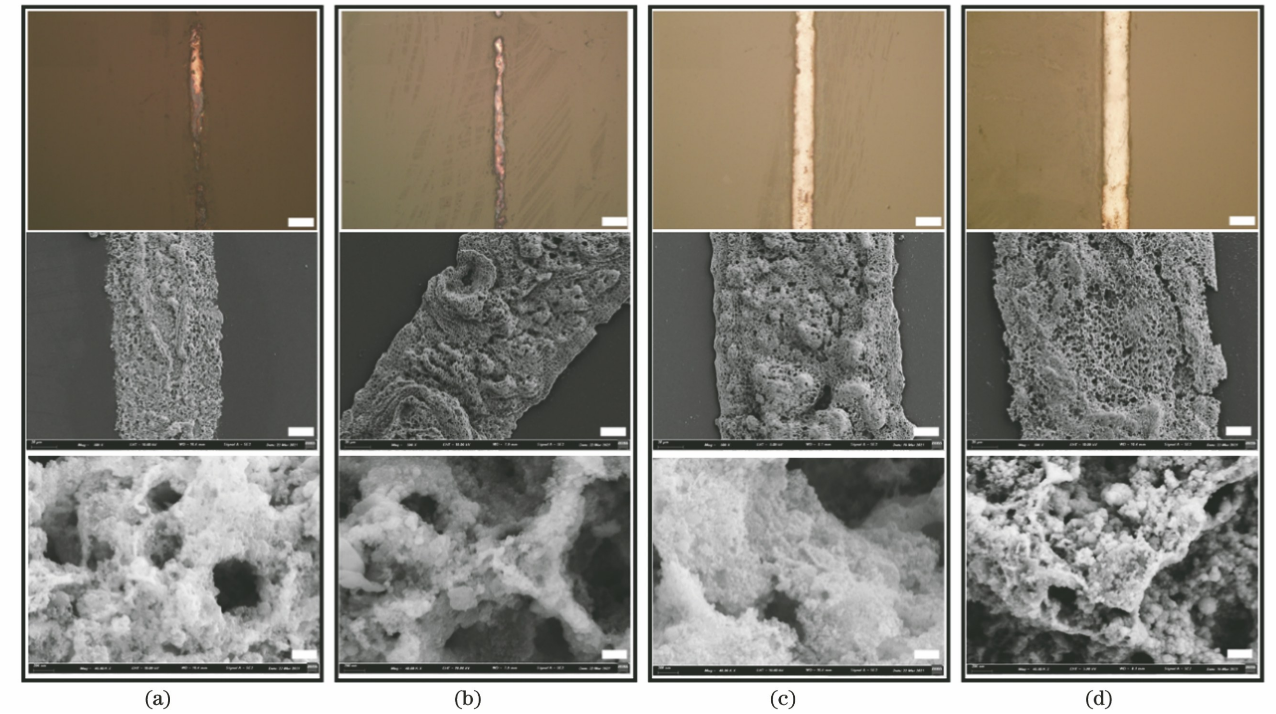

图 2　扫描速度为 500 mm・s^{-1} 时，在不同光强下制备的铜微结构的 OM、SEM 及高倍 SEM 照片。(a) 5.32×10^{9} W・cm^{-2}；(b) 6.38×10^{9} W・cm^{-2}；(c) 7.45×10^{9} W・cm^{-2}；(d) 8.51×10^{9} W・cm^{-2}（OM 照片标尺为 100 μm，低倍 SEM 照片标尺为 20 μm，高倍 SEM 照片标尺为 200 nm）

Fig. 2　OM, SEM and high-resolution SEM images of copper microstructures obtained under different intensities with a constant scanning speed of 500 mm·s^{-1}. (a) 5.32×10^{9} W·cm^{-2}; (b) 6.38×10^{9} W·cm^{-2}; (c) 7.45×10^{9} W·cm^{-2}; (d) 8.51×10^{9} W·cm^{-2} (the scale bars are 100 μm, 20 μm and 200 nm in OM, SEM and high-resolution SEM images, respectively)

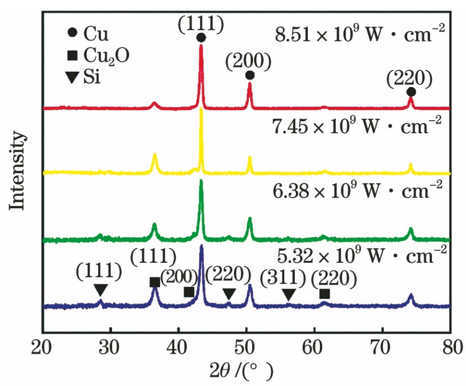

图 3　扫描速度为 500 mm・s^{-1} 时，在不同光强下制备的铜微结构的 XRD 图谱

Fig. 3　XRD spectra of copper microstructures obtained under different intensities with a constant scanning speed of 500 mm·s^{-1}

(111)、(200)和(220)面对应，36.4°、42.3°和 61.4°处的三个衍射峰分别与 Cu_2O 的(111)、(200)和(220)面对应。当激光光强低于 6.38×10^{9} W・cm^{-2} 时，XRD 图谱上可以观察到较弱的硅相的衍射峰，峰位分别位于 28.4°、47.3°和 56.1°，分别对应于(111)、(200)和(311)面。此时激光光强较低，不足以使前驱体溶液中的 Cu^{2+} 完全还原为金属铜，剩余的 Cu^{2+} 被还原为 Cu_2O。金属铜、未彻底还原的 Cu_2O 以及分散在溶液中的硅纳米颗粒一起沉积在基底表面。随着光强增加，Cu_2O 相的峰强逐渐减弱，铜相的峰强逐渐增强，表明更多的 Cu^{2+} 被还原为金属铜；同时，由于被还原的金属铜相远多于硅相，因此硅相的衍射峰逐渐被掩盖。

与已有飞秒激光直写铜微结构的研究（光强为 $10^{11}\sim10^{12}$ W・cm^{-2} 量级）[25-27] 相比，本文所提在前驱体溶液中添加吸光纳米颗粒后的方法可使飞秒激光的光强降低。图 4(a)为激光辐照未添加吸光粒子的前驱体溶液时发生还原反应的原理图。激光光强在溶液内部沿激光入射方向逐渐降低，部分激光能量被溶液吸收，溶液内形成了一定范围的热还原反应区，反应区内的 Cu^{2+} 发生还原反应。在前驱体溶液中添加吸光纳米颗粒后的还原反应原理图如图 4(b)所示。吸光粒子硅的禁带宽度为 1.12 eV，远小于波长为 515 nm 入射激光的光子能量（约

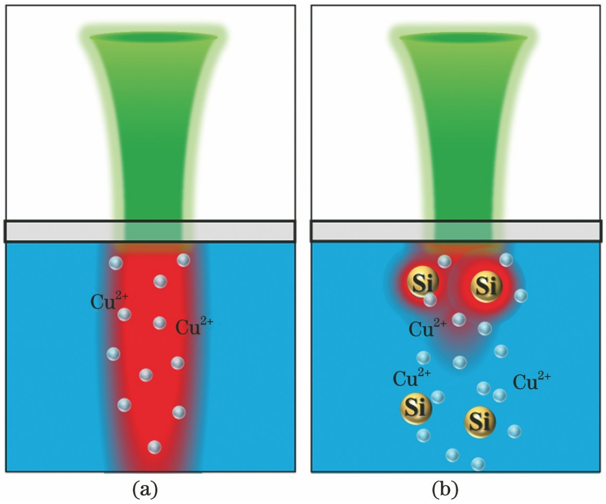

图 4　飞秒激光直写铜微结构发生还原反应的示意图。(a)未添加吸光粒子；(b)添加吸光粒子

Fig. 4　Schematics of reduction reaction during femtosecond laser direct writing of copper microstructures. (a) Without photon-absorbing nanoparticles; (b) with photon-absorbing nanoparticles

2.41 eV)。当激光辐照前驱体溶液时，分散在溶液中的纳米硅颗粒吸收激光能量后加热周围的溶液，形成分散的局部热还原区，使其周围的 Cu^{2+} 发生还原反应。与未添加 Si 颗粒的溶液相比，硅颗粒的添加缩短了入射激光的穿透深度，在相同的光强下，发生光热还原区域的溶液体积减少、温度更高，在低光强下更多的 Cu^{2+} 被还原为单质铜。

3.2　扫描速度对铜微结构形貌及物相的影响

如前所述，当激光光强为 5.32×10^{9} W・cm^{-2}、扫描速度为 500 mm・s^{-1} 时，基底表面开始沉积少量金属铜。保持光强为 5.32×10^{9} W・cm^{-2} 不变，不同扫描速度下的铜微结构的形貌如图 5 所示。从低倍率 OM 照片中可以看出，当扫描速度为 100～400 mm・s^{-1} 时，基底表面形成了连续的铜微结构，微结构的线宽随着扫描速度的降低而逐渐增加。这是由于在光强一定的情况下，随着扫描速度减小，激光与溶液作用时间增加，被彻底还原的 Cu^{2+} 增多，沉积的金属铜增多，因此线宽增加。当扫描速度为 100 mm・s^{-1} 时，微结构的线宽为 225 μm，小于光斑直径。进一步，利用 SEM 观察了不同扫描速度下铜微结构的表面形貌，结果发现不同扫描速度下的铜微结构整体上很相似，均呈三维网络状结构。

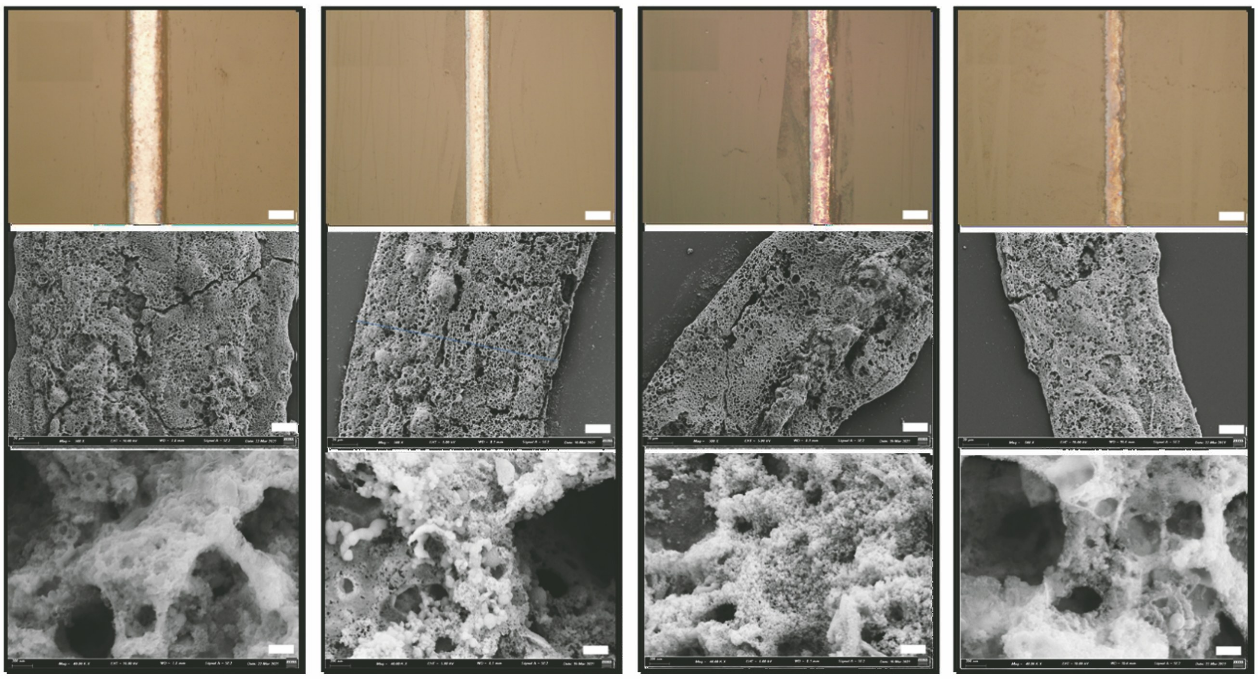

图 5　光强为 5.32×10^{9} W・cm^{-2} 时，在不同扫描速度下制备的铜微结构的 OM、SEM 及高倍 SEM 照片。(a) 100 mm・s^{-1}；(b) 200 mm・s^{-1}；(c) 300 mm・s^{-1}；(d) 400 mm・s^{-1}(OM 标尺为 100 μm，SEM 标尺为 20 μm，高倍 SEM 标尺为 200 nm)

Fig. 5　OM, SEM and high-resolution SEM images of copper microstructures obtained under different scanning speeds with a laser intensity of 5.32×10^{9} W・cm^{-2}. (a) 100 mm・s^{-1}; (b) 200 mm・s^{-1}; (c) 300 mm・s^{-1}; (d) 400 mm・s^{-1} (the scale bars are 100 μm, 20 μm and 200 nm in OM, SEM and high-resolution SEM images, respectively)

图 6 为激光直写微结构的物相与 XRD 图谱(激光功率为 5.32×10^9 W·cm^{-2},扫描速度为 100~400 mm·s^{-1})。从图 6(a)可以看出,在不同的扫描速度下,微结构主要由金属铜相、Cu_2O 相以及微量硅相组成,与不同光强下制备的微结构的成分相似。各相的比例随着扫描速度的变化而改变,具体变化情况如图 6(b)所示。当扫描速度由 400 mm·s^{-1} 降低至 100 mm·s^{-1} 时,金属铜相的占比由 64.6%提高至 89.7%,Cu_2O 相由 28.6%降低至 4.8%,硅相由 6.8%降低至 5.5%。这是由于当扫描速度较快时,激光与溶液的作用时间较短,部分 Cu^{2+} 没有被彻底还原为金属铜,而是转化为中间产物 Cu_2O。随着扫描速度的降低,激光与溶液作用时间延长,更多的 Cu^{2+} 被彻底还原为单质铜,少部分被还原为 Cu_2O。

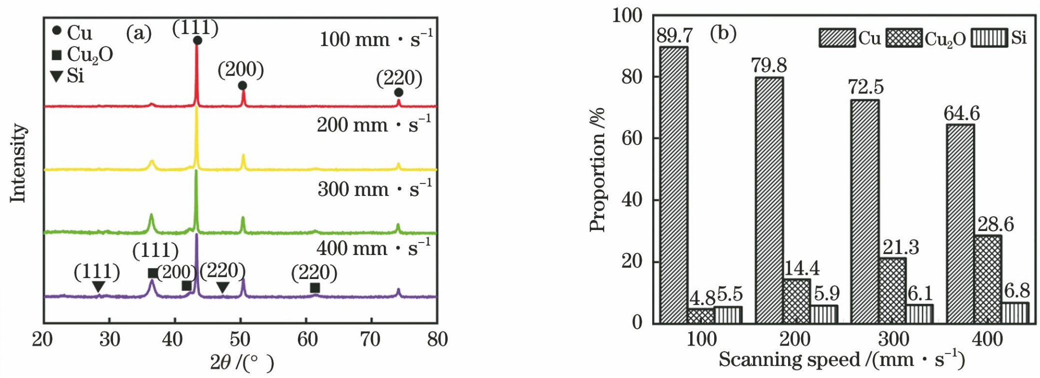

图 6 光强为 5.32×10^9 W·cm^{-2} 时,在不同扫描速度下制备的铜微结构的 XRD 图谱以及各相的占比。(a)XRD 图谱;(b)各相的占比

Fig. 6 XRD spectra and proportion of each phase in copper microstructure obtained under different scanning speeds with a laser intensity of 5.32×10^9 W·cm^{-2}. (a) XRD spectra; (b) proportion of each phase

与已有的飞秒激光直写金属铜的研究结果相比,本文中基于吸光粒子热效应的直写方法可以显著提高微结构的直写效率。为了方便比较,本文将直写效率定义为单位时间内直写金属的体积(μm^3·s^{-1})。表 1 所示为计算得到的铜微结构的直写效率与文献数据的对比。可以看出,本文所提直写方法的效率远大于已有文献中的直写效率,较之提高了 1~3 个数量级。

表 1 金属铜微结构飞秒激光直写效率的对比

Table 1 Comparison of direct writing efficiency of femtosecond laser direct writing of Cu microstructures

Method	Max. scanning speed /(mm·s^{-1})	Max. line width /μm	Thickness /μm	Writing efficiency /(μm^3·s^{-1})
Method in Ref. [27]	5	~30	0.64 (glass substrate)	9.6×10^4
	10	~50	1.7 (PDMS substrate)	8.5×10^5
Method in Ref. [28]	8	~5	7	2.8×10^5
Method in Ref. [29]	5	~40	<6	1.2×10^6
Method in Ref. [25]	1	~20	0.6	1.2×10^4
Our method	500 (repeated 50 times)	225	~17	3.83×10^7

3.3 飞秒激光直写铜微结构的导电性

根据前文的研究,激光光强和激光扫描速度的变化会影响溶液中发生还原反应区域的温度,从而最终影响铜微结构的形貌与物相。当光强为 5.32×10^9 W·cm^{-2} 时,铜微结构的方阻随激光扫描速度的变化如图 7(a)所示。总体上,微结构的方阻随扫描速度的增加而增加。当扫描速度较快(500 mm·s^{-1})时,直写微结构的方阻超过了 0.5 MΩ·sq^{-1}。这由于前驱体溶液中只还原出了分散的铜纳米颗粒,直写结构不连续,如图 2(a)所示,同时 Cu_2O 的含量较高,导致铜微结构的方阻较大。当扫描速度降低至 400 mm·s^{-1} 时,方阻迅速降低至 70.90 Ω·sq^{-1},下降了 4 个数量级。这是由于随着扫描速度降低,基底表面形成了连续的微结构,如图 5(d)所示,同时微结构中的铜含量增加,因此微结构的导电性明显提高。当扫描速率降低至

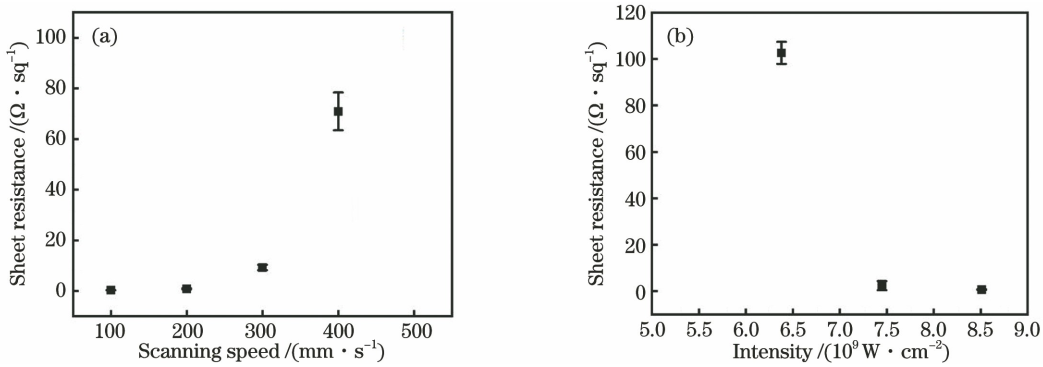

图 7 铜微结构方阻随激光参数的变化。(a)随扫描速度的变化,光强为 5.32×10^{9} W·cm^{-2};(b)随光强的变化,扫描速度为 500 mm·s^{-1}

Fig. 7 Variation of sheet resistance of copper microstructures with laser parameters. (a) Variation with scanning speed under a constant laser intensity of 5.32×10^{9} W·cm^{-2}; (b) variation with laser intensity at a constant scanning speed of 500 mm·s^{-1}

100 mm·s^{-1} 时,微结构的方阻降低至 0.28 Ω·sq^{-1},优于目前大部分激光直写金属铜材料的导电薄膜(0.57～1.3 Ω·sq^{-1})[30-32]以及溶液法制备的铜纳米线导电薄膜(17 Ω·sq^{-1})[33]。当扫描速度为 500 mm·s^{-1} 时,微结构的方阻随光强的变化如图 7(b)所示,可以看出,微结构的方阻随着光强的增加而逐渐降低。这是由于随着激光光强增加,微结构逐渐形成了连续结构,同时铜含量逐渐增加。当光强为 8.51×10^{9} W·cm^{-2} 时,方阻降低至 0.52 Ω·sq^{-1},为低光强低扫描速度下方阻的 2 倍。

激光直写微结构的表面均匀性和厚度会影响其方阻的大小。图 8 是当光强为 5.32×10^{9} W·cm^{-2} 时,不同扫描速度下飞秒激光直写铜微结构的三维形貌。当扫描速度为 400 mm·s^{-1} 时,由于激光辐射区域单位面积内的激光能量较少,微结构厚度较薄,约为 5.99 μm,微结构表面不均匀且边缘不平整,如图 8(a)所示。随着扫描速度降低,微结构的厚度逐渐增大,当扫描速度降为 100 mm·s^{-1} 时,微结构的平均厚度为 16.92 μm,微结构表面均匀且边缘清晰,如图 8(d)所示。当扫描速度为 500 mm·s^{-1} 时,基底表面无法形成连续的铜微结构,导致方阻(>0.5 MΩ·sq^{-1})超过四探针测试仪的量程。不同扫描速度下微结构的方阻、厚度及相应的电阻率见表2。微结构的优异导电性能表明,前驱体溶

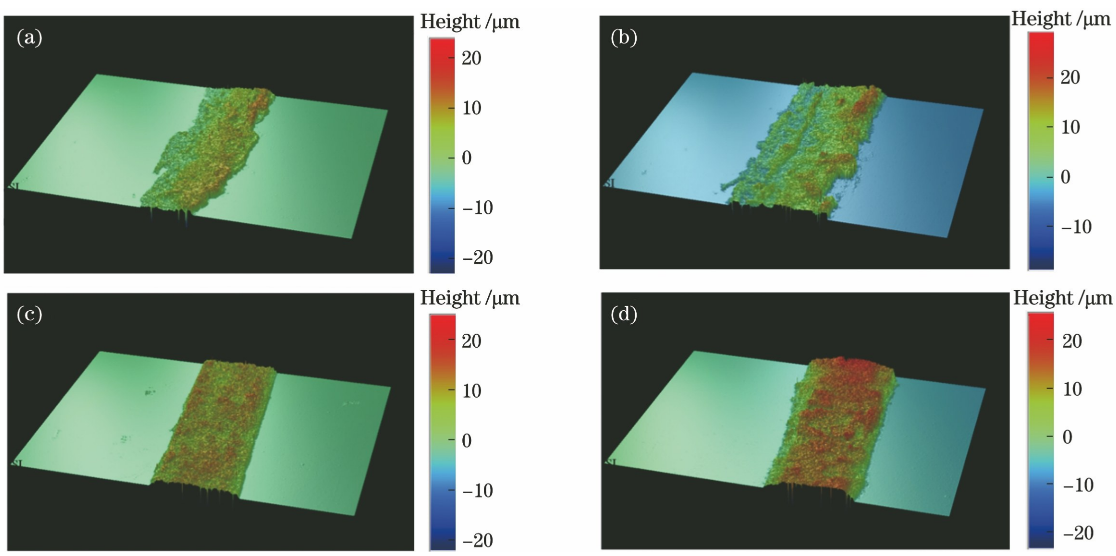

图 8 当光强为 5.32×10^{9} W·cm^{-2} 时,不同扫描速度下飞秒激光直写铜微结构的三维形貌。(a) 400 mm·s^{-1};(b) 300 mm·s^{-1};(c) 200 mm·s^{-1};(d) 100 mm·s^{-1}

Fig. 8 Three-dimensional morphologies of copper microstructures prepared by femtosecond laser direct writing under different scanning speeds with a constant laser intensity of 5.32×10^{9} W·cm^{-2}. (a) 400 mm·s^{-1}; (b) 300 mm·s^{-1}; (c) 200 mm·s^{-1}; (d) 100 mm·s^{-1}.

表 2 不同扫描速度下飞秒激光直写铜微结构的方阻、厚度及电阻率

Table 2 Sheet resistivity, thickness, and electrical resistivity of femtosecond laser direct written Cu microstructures at different scanning speeds

Scanning speed /(mm·s^{-1})	Sheet resistance /(Ω·sq^{-1})	Thickness / μm	Electrical resistivity /(Ω·m)
100	0.28±0.01	16.92±5.45	4.67×10^{-6}
200	0.83±0.22	11.83±2.74	9.82×10^{-6}
300	9.26±1.07	10.79±1.83	9.98×10^{-5}
400	70.90±7.47	5.99±3.79	4.25×10^{-4}
500	$>0.5\times10^{6}$		

液中添加的硅纳米颗粒不会影响金属微结构的导电率，相反，添加的硅纳米吸光粒子改变了激光与前驱体溶液相互作用区域的体积，提高了微结构中的铜含量，从而提高了直写微结构的导电性。

本文提出的飞秒激光直写方法实现了线宽小于光斑直径的金属微结构的制造，如图 2 和图 5 所示。由于飞秒激光的阈值效应，光热效应诱导 Cu^{2+} 还原反应只发生在光强超过一定阈值的区域，如图 9 所示。连续、普通脉冲或短脉冲激光直写金属微结构时无法精确控制热输入量，激光热累积明显，导致金属微结构的线宽大于光斑直径[11,34]。飞秒激光可以精确控制激光的热输入量，将发生光热反应的区域限制在很小的区域内，从而可以获得线宽小于光斑直径的微结构。理论上，光斑直径只受光学衍射极限的限制，即只受激光波长(λ)和数值孔径(NA)的限制。根据瑞利判据，光学系统的分辨率 $d=0.61\lambda/NA$，常见的较大 NA 为 1.4，因此理论上最小的铜微结构线宽小于 0.44λ。本文选用的激光波长为 515 nm，因此，金属微结构的最小线宽有望达到 220 nm。

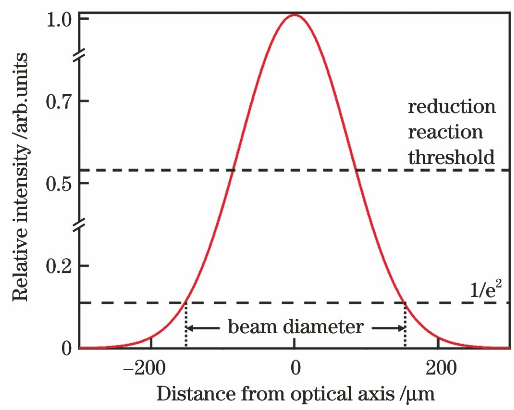

图 9 飞秒激光直写金属铜微结构的阈值效应示意图

Fig. 9 Schematic of threshold effect during femtosecond laser direct writing of copper microstructures

当激光光强为 7.45×10^{9} W·cm^{-2}、扫描速度为 500 mm·s^{-1}、填充间距为 25 μm 时，不同图案二维微结构的照片如图 10 所示。图 10(a)为飞秒激光直写的二维方形铜薄膜，其尺寸为 10 mm×10 mm。图 10(b)为飞秒激光直写的铜薄膜太极图案。飞秒激光直写的金属二维图形表明该技术具有柔性化制造的特点。

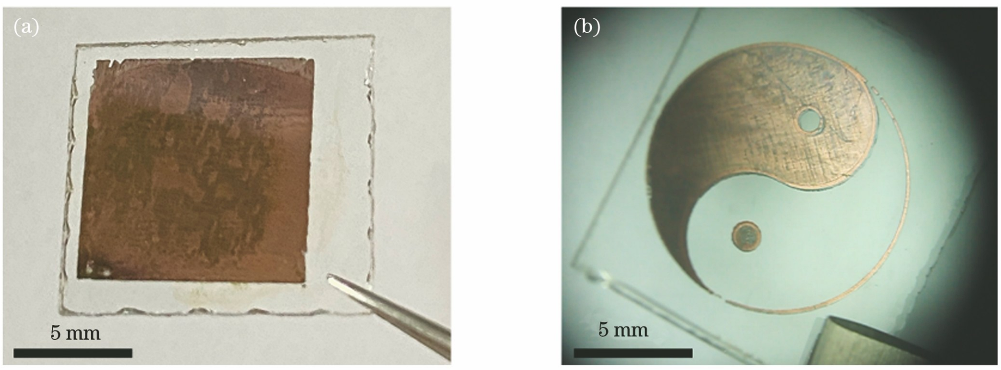

图 10 飞秒激光直写不同图案二维铜薄膜的照片。(a) 10 mm×10 mm 的方形图案；(b)太极图案

Fig. 10 Digital images of two-dimensional Cu film pattern prepared using femtosecond laser direct writing. (a) Square pattern with size of 10 mm×10 mm; (b) Tai Chi pattern

4　结　论

本课题组在前驱体溶液中添加硅纳米吸光粒子，利用飞秒激光直写技术在玻璃表面制备了导电金属铜微结构。研究结果如下：

1）当光强为 5.32×10^9～8.51×10^9 W·cm^{-2}、扫描速度为 100～500 mm·s^{-1} 时，采用飞秒激光实现了在玻璃表面直写铜微结构，微结构主要由铜、Cu_2O 及微量硅组成；随着光强增加或扫描速度降低，微结构的连续性和铜含量增加。

2）当光强为 5.32×10^9 W·cm^{-2} 时，方阻和电阻率均随扫描速度的降低而显著降低，当扫描速度为 100 mm·s^{-1} 时，飞秒激光直写铜微结构具有优异的导电性能，方阻降低至 0.28 Ω·sq^{-1}，电阻率降低至 4.67×10^{-6} Ω·m。

3）与已有的研究结果相比，这种方法使飞秒激光直写铜微结构的光强降低了 2 个数量级，效率提高了 1～3 个数量级；

4）这种方法可以获得线宽小于光斑直径的微结构。

参　考　文　献

[1] Siebert L, Wolff N, Ababii N, et al. Facile fabrication of semiconducting oxide nanostructures by direct ink writing of readily available metal microparticles and their application as low power acetone gas sensors[J]. Nano Energy, 2020, 70: 104420.

[2] Bhuiyan M E H, Behroozfar A, Daryadel S, et al. A hybrid process for printing pure and high conductivity nanocrystalline copper and nickel on flexible polymeric substrates[J]. Scientific Reports, 2019, 9(1): 19032.

[3] Jin W Y, Ovhal M M, Lee H B, et al. Scalable, all-printed photocapacitor fibers and modules based on metal-embedded flexible transparent conductive electrodes for self-charging wearable applications[J]. Advanced Energy Materials, 2021, 11(4): 2003509.

[4] Semple J, Georgiadou D G, Wyatt-Moon G, et al. Large-area plastic nanogap electronics enabled by adhesion lithography[J]. Npj Flexible Electronics, 2018, 2: 18.

[5] Alhendi M, Sivasubramony R S, Weerawarne D L, et al. Assessing current-carrying capacity of aerosol jet printed conductors[J]. Advanced Engineering Materials, 2020, 22(11): 2000520.

[6] Wang X L, Liu J. Recent advancements in liquid metal flexible printed electronics: properties, technologies, and applications[J]. Micromachines, 2016, 7(12): 206.

[7] Cong H L, Xu X D, Yu B, et al. Recent progress in preparation and application of microfluidic chip electrophoresis[J]. Journal of Micromechanics and Microengineering, 2015, 25(5): 053001.

[8] Shi Y, Xu B, Wu D, et al. Research progress on fabrication of functional microfluidic chips using femtosecond laser direct writing technology[J]. Chinese Journal of Lasers, 2019, 46(10): 1000001.
史杨, 许兵, 吴东, 等. 飞秒激光直写技术制备功能化微流控芯片研究进展[J]. 中国激光, 2019, 46(10): 1000001.

[9] Zhou X W, Liao J N, Yao Y, et al. Direct laser writing of micro/nano copper structures and their applications[J]. Chinese Journal of Lasers, 2021, 48(8): 0802012.
周兴汶, 廖嘉宁, 姚煜, 等. 铜微纳结构的激光直写及其应用研究进展[J]. 中国激光, 2021, 48(8): 0802012.

[10] Chen Z Y, Fang G, Cao L C, et al. Direct writing of silver micro-nanostructures by femtosecond laser tweezer[J]. Chinese Journal of Lasers, 2018, 45(4): 0402006.
陈忠贇, 方淦, 曹良成, 等. 飞秒激光光镊直写银微纳结构[J]. 中国激光, 2018, 45(4): 0402006.

[11] Seo J M, Kwon K K, Song K Y, et al. Deposition of durable micro copper patterns into glass by combining laser-induced backside wet etching and laser-induced chemical liquid phase deposition methods[J]. Materials, 2020, 13(13): 2977.

[12] Zarzar L D, Swartzentruber B S, Donovan B F, et al. Using laser-induced thermal voxels to pattern diverse materials at the solid-liquid interface[J]. ACS Applied Materials & Interfaces, 2016, 8(33): 21134-21139.

[13] Pique A, Arnold C B, Pratap B, et al. Laser direct-write of metal patterns for interconnects and antennas[J]. Proceedings of SPIE, 2003, 4977: 602-608.

[14] Paeng D, Lee D, Yeo J, et al. Laser-induced reductive sintering of nickel oxide nanoparticles under ambient conditions[J]. The Journal of Physical Chemistry C, 2015, 119(11): 6363-6372.

[15] Toriyama S, Mizeikis V, Ono A. Fabrication of silver nano-rings using photo-reduction induced by femtosecond pulses[J]. Applied Physics Express, 2019, 12(1): 015004.

[16] Lu W E, Zhang Y L, Zheng M L, et al. Femtosecond direct laser writing of gold

nanostructures by ionic liquid assisted multiphoton photoreduction[J]. Optical Materials Express, 2013, 3(10): 1660-1673.

[17] Ren S T, Wang Q, Wang Y S, et al. Three distinct hydrogen sensing responses of palladium line patterns generated by femtosecond laser direct writing [J]. Journal of Physics D, 2012, 45(28): 285303.

[18] Bai S, Zhang S G, Zhou W P, et al. Laser-assisted reduction of highly conductive circuits based on copper nitrate for flexible printed sensors[J]. Nano-Micro Letters, 2017, 9(4): 1-13.

[19] Kim D, Choi C. Laser-induced metal reduction from liquid electrolyte precursor[J]. Journal of Nanoscience and Nanotechnology, 2013, 13(11): 7581-7585.

[20] Wang X C, Zheng H Y, Lim G C. Laser direct writing of copper on polyimide, FR4, and Al_2O_3 substrates from solid-metalorganic film[J]. Proceedings of SPIE, 2001, 4274: 403-410.

[21] Greenberg E, Armon N, Kapon O, et al. Nanostructure and mechanism of metal deposition by a laser-induced photothermal reaction[J]. Advanced Materials Interfaces, 2019, 6(14): 1900541.

[22] Cao Y Y, Takeyasu N, Tanaka T, et al. 3D metallic nanostructure fabrication by surfactant-assisted multiphoton-induced reduction [J]. Small, 2009, 5 (10): 1144-1148.

[23] Xu B B, Xia H, Niu L G, et al. Flexible nanowiring of metal on nonplanar substrates by femtosecond-laser-induced electroless plating[J]. Small, 2010, 6 (16): 1762-1766.

[24] Long J, Jiao F Z, Fan X H, et al. Femtosecond laser assembly of one-dimensional nanomaterials and their application[J]. Chinese Journal of Lasers, 2021, 48 (2): 0202017.
龙婧, 焦玢璋, 范旭浩, 等. 飞秒激光组装一维纳米材料及其应用[J]. 中国激光, 2021, 48(2): 0202017.

[25] Mizoshiri M, Aoyama K, Uetsuki A, et al. Direct writing of copper micropatterns using near-infrared femtosecond laser-pulse-induced reduction of glyoxylic acid copper complex[J]. Micromachines, 2019, 10 (6): 401.

[26] Liao J N, Wang X D, Zhou X W, et al. Joining process of copper nanoparticles with femtosecond laser irradiation[J]. Chinese Journal of Lasers, 2021, 48(8): 0802008.
廖嘉宁, 王欣达, 周兴汶, 等. 铜纳米颗粒的飞秒激光连接过程研究[J]. 中国激光, 2021, 48(8): 0802008.

[27] Ha N, Ohishi T, Mizoshiri M. Direct writing of Cu patterns on polydimethylsiloxane substrates using femtosecond laser pulse-induced reduction of glyoxylic acid copper complex[J]. Micromachines, 2021, 12(5): 493.

[28] Mizoshiri M, Yoshidomi K. Cu patterning using femtosecond laser reductive sintering of CuO nanoparticles under inert gas injection[J]. Materials, 2021, 14(12): 3285.

[29] Chong P Y, Ho J R. Electrical and microstructure characteristics of SU_8-Cu composite thin film fabricated using femtosecond laser direct writing[J]. Applied Physics A, 2020, 126(5): 372.

[30] Zhou X W, Guo W, Yao Y, et al. Flexible nonenzymatic glucose sensing with one-step laser-fabricated Cu_2O/Cu porous structure[J]. Advanced Engineering Materials, 2021: 2100192.

[31] Liao J N, Guo W, Peng P. Direct laser writing of copper-graphene composites for flexible electronics [J]. Optics and Lasers in Engineering, 2021, 142: 106605.

[32] Zhou X W, Guo W, Fu J, et al. Laser writing of Cu/Cu_xO integrated structure on flexible substrate for humidity sensing[J]. Applied Surface Science, 2019, 494: 684-690.

[33] Park J H, Han S, Kim D, et al. Plasmonic-tuned flash Cu nanowelding with ultrafast photochemical-reducing and interlocking on flexible plastics [J]. Advanced Functional Materials, 2017, 27(29): 1701138.

[34] Peng P, Li L H, He P, et al. One-step selective laser patterning of copper/graphene flexible electrodes [J]. Nanotechnology, 2019, 30(18): 185301.

Femtosecond Laser Direct Writing of Copper Microstructures with High Efficiency via Thermal Effect of Nanoparticles

Cui Mengya, Huang Ting*, Xiao Rongshi

Faculty of Materials and Manufacturing, Beijing University of Technology, Beijing 100124, *China*

Abstract

Objective The precise conductive Cu micropatterns have been used in a variety of electronic devices. Compared to other traditional fabrication methods, laser direct writing is more efficient and reliable. The femtosecond laser direct writing technique, in particular, is used to construct highly conductive Cu microstructures. Femtosecond laser with ultrashort pulse duration can precisely control the heat input resulting in the reduction of Cu^{2+} in the laser irradiation zone without the damage of substrate. However, the intensity is as high as 10^{11} $W\cdot cm^{-2}$ and the scanning speed is generally lower than 10 $mm\cdot s^{-1}$ to achieve the necessary reduction temperature. Si nanoparticles were added to Cu^{2+} solution in this study, acting as photon-absorbing nanoparticles due to their narrow band-gap. The photon-absorbing nanoparticles reduced the volume of the reduction zone by decreasing the penetration depth. The temperature of the reduction zone was rising, resulting in more efficient and less expensive direct writing. As a result, the conductive Cu microstructures were deposited on the substrate with the intensity from 5.32×10^9 to 8.51×10^9 $W\cdot cm^{-2}$ and the scanning speed from 100 to 500 $mm\cdot s^{-1}$. The intensity was two orders of magnitude lower, and the direct writing efficiency was three orders of magnitude higher, compared to previously reported work. The impacts of scanning speed and intensity on the morphology, chemical composition, and conductivity of Cu microstructures were investigated. The lowest sheet resistance was 0.28 $\Omega\cdot sq^{-1}$ and the lowest electrical resistivity was 4.67×10^{-6} $\Omega\cdot m$ at the intensity of 5.32×10^9 $W\cdot cm^{-2}$ with a scanning speed of 100 $mm\cdot s^{-1}$, respectively.

Methods The solvent was prepared by mixing 6 mL of ethylene glycol and 3 mL of deionized water. 4 g of $Cu(NO_3)_2\cdot 3H_2O$ was added to the solvent with ultrasonication for at least 30 min to thoroughly dissolve $Cu(NO_3)_2\cdot 3H_2O$. For 2 minutes, the liquid was heated to 170 ℃. The solvent received 100 mg of Si nanoparticles. To obtain the suspension liquid, the mixed solution was ultrasonically homogenized for 1 h. Glass was used as a substrate that was adhered to the suspension liquid's surface. The laser beam scanning was controlled by a femtosecond laser equipped with a galvanometer system. After the femtosecond laser irradiation, the conductive Cu microstructure was formed on the backside of the substrate. Then, the morphologies of the Cu microstructures were characterized by optical microscopy and field emission scanning electron microscopy. The composition of the Cu microstructures was verified using X-ray diffraction. The thickness of the microstructures was measured and the three-dimensional topography of the microstructures was depicted using a surface profiler. Cu microstructures' electrical properties were measured using a source meter based on the four-point probe method.

Results and Discussions The continuity of laser-fabricated microstructures and the proportion of Cu increased with the increasing intensity (Fig. 2 and Fig. 3). The intensity was two orders of magnitude lower than that in previous experiments. The addition of photon-absorbing Si nanoparticles to the suspension liquid resulted in a decrease in laser penetration depth in solution, raising the temperature of the laser-induced reduction zone (Fig. 4). The more metallic Cu was obtained. The continuity of microstructures and the proportion of Cu also increased with the decreasing scanning speed (Fig. 5 and Fig. 6). The direct writing efficiency was one to three orders of magnitude higher than that in previous work (Table 1). The sheet resistance and electrical resistivity of as-fabricated Cu microstructures tended to decrease with increasing intensity or decreasing scanning speed (Fig. 7). The Cu microstructure obtained at 5.32×10^9 $W\cdot cm^{-2}$ intensity and 100 $mm\cdot s^{-1}$ scanning speed exhibited the lowest sheet resistance of 0.28 $\Omega\cdot sq^{-1}$. Moreover, as a result of the reduction reaction threshold, the microstructure's line width was narrower than the laser spot's diameter. As a result, the heat input to the irradiation zone was precisely controlled, limiting the reduction zone area and resulting in finer line width formation (Fig. 9).

Conclusions In this study, highly conductive Cu microstructures were formed on a glass substrate using femtosecond laser direct writing. As photon-absorbing nanoparticles, Si nanoparticles were added to the precursor solution. With the intensity ranging from 5.32×10^9 $W\cdot cm^{-2}$ to 8.51×10^9 $W\cdot cm^{-2}$ and the scanning speed ranging from 100 mm·s^{-1} to 500 mm·s^{-1}, the Cu microstructures were formed on substrates. Metallic copper, Cu_2O, and minor Si were found in the copper microstructures. The results show that the continuity of the microstructure, the proportion of Cu, and the conductivity of the microstructures all increased with increasing intensity or decreasing scanning speed. At the scanning speed of 100 mm·s^{-1}, the lowest sheet resistance of 0.28 Ω·sq^{-1} and the lowest electrical resistivity of 4.67×10^{-6} Ω·m were obtained. The intensity was two orders of magnitude lower than that in previous work, and the direct writing efficiency was one to three orders of magnitude higher than that in previous work. Moreover, the line width of the microstructure was significantly smaller than the diameter of the laser spot.

Key words laser technique; femtosecond laser; laser direct writing; photon-absorbing nanoparticles; copper microstructure; electrical conductivity